IMPROVING THE SPACE SURVEILLANCE TELESCOPE'S PERFORMANCE USING MULTI-HYPOTHESIS TESTING

The Astronomical Journal, 147:111 (13pp), 2014 May doi:10.1088/0004-6256/147/5/111

IMPROVING THE SPACE SURVEILLANCE TELESCOPE'S PERFORMANCE USING MULTI-HYPOTHESIS TESTING*

J. Chris Zingarelli[1], Eric Pearce[2], Richard Lambour[2], Travis Blake[3], Curtis J. R. Peterson[4], and Stephen Cain[1]
[1] Air Force Institute of Technology, 2950 Hobson Way, Bldg 641, Wright Patterson AFB, OH 45433, USA; John.Zingarelli@afit.edu
[2] Lincoln Labratory, Massachusetts Institute of Technology, 244 Wood Street, Lexington, MA 02421, USA
[3] Defense Advanced Research Projects Agency, 675 North Randolph Street Arlington, VA 22203, USA
[4] United States Air Force, 1690 Air Force Pentagon, Washington, DC 20330, USA
Received 2013 March 22; accepted 2014 February 22; published 2014 April 10

ABSTRACT

The Space Surveillance Telescope (SST) is a Defense Advanced Research Projects Agency program designed to detect objects in space like near Earth asteroids and space debris in the geosynchronous Earth orbit (GEO) belt. Binary hypothesis test (BHT) methods have historically been used to facilitate the detection of new objects in space. In this paper a multi-hypothesis detection strategy is introduced to improve the detection performance of SST. In this context, the multi-hypothesis testing (MHT) determines if an unresolvable point source is in either the center, a corner, or a side of a pixel in contrast to BHT, which only tests whether an object is in the pixel or not. The images recorded by SST are undersampled such as to cause aliasing, which degrades the performance of traditional detection schemes. The equations for the MHT are derived in terms of signal-to-noise ratio (S/N), which is computed by subtracting the background light level around the pixel being tested and dividing by the standard deviation of the noise. A new method for determining the local noise statistics that rejects outliers is introduced in combination with the MHT. An experiment using observations of a known GEO satellite are used to demonstrate the improved detection performance of the new algorithm over algorithms previously reported in the literature. The results show a significant improvement in the probability of detection by as much as 50% over existing algorithms. In addition to detection, the S/N results prove to be linearly related to the least-squares estimates of point source irradiance, thus improving photometric accuracy.

Key words: atmospheric effects – methods: data analysis – telescopes

Online-only material: color figures

1. INTRODUCTION

Through the National Aeronautics and Space Administration (NASA) Multiyear Authorization Act of 1990 and the NASA Authorization Act of 2005, the U.S. Congress mandated NASA, in coordination with the Department of Defense and other international space agencies, to catalog by the year 2020, 90% of all asteroids and comets larger than 140 m whose trajectory brings them close to the orbit of Earth (Congress 2005). Congress also directed NASA to submit an Analysis of Alternatives (AoA) outlining their efforts to detect and characterize the hazards of near Earth asteroids (NEAs), as well as an assessment of necessary actions to put in place capabilities to expand the detection and tracking of NEAs. The AoA details two considered terrestrial sensors, as well as several space-based systems. The two terrestrial-based systems are the Large Synoptic Survey Telescope (LSST) and the Panoramic Survey Telescope and Rapid Response System (Pan-STARRS). The AoA reported that a program consisting of a combination of both ground-based systems and some space-based systems was required to meet the 2020 deadline for completion. The AoA also reported that using only one of the land-based systems would push the date out to beyond 2030 (National Aeronautics and Space Administration 2007). As of 2011 July 15, fewer than 900 of the estimated 1100 NEAs larger than 1 km have been discovered, and fewer than 5000 of the estimated 100,000 NEAs between 100 m and 1 km have been discovered and cataloged (National Aeronautics and Space Administration 2011).

In 1984, the University of Arizona's Spacewatch team developed the drift-scan and step-stare methods used by many of the astronomical observing telescopes today to automatically detect moving objects (http://spacewatch.lpl.arizona.edu/index.html). Since the Spacewatch program, at least five subsequent NEA detection programs have used, or are using, the step-stare method in order to detect moving objects. These programs include the Near Earth Asteroid Tracking, Lincoln Near Earth Asteroid Research (LINEAR), Lowell Observatory Near Earth Object Search, Catalina Sky Survey, and the Japanese Spaceguard Association programs (Stokes et al. 2002). Two time-domain matched filter approaches to asteroid detection are described in Miura & Itagaki (2005) and Gural et al. (2005); however, these particular approaches are not investigated in this paper because the time-domain match filters operate on the trajectory of the object over time as opposed to the spatial shape of the object in a single observation. Pan-STARRS currently uses a different matched filter approach for asteroid detection. It has implemented the first major change in NEA detection methods since the drift-scan and step-stare methods by creating a running average, or "master image" of the sky and using it in an image differencing algorithm together with a spatial matched-filter (LSST Corporation 2011). LSST plans to use both the step-stare approach and an image difference detection requiring the most comprehensive and sophisticated star chart catalog to be built and used in a similar manner as Pan-STARRS's master image (Magnier 2007).

Recently, the Defense Advanced Research Projects Agency (DARPA) has been commissioned by NASA to provide data from its 3.5 m Space Surveillance Telescope (SST), located at White Sands Missile Range, NM, for use in detecting and

* The views expressed are those of the author and do not reflect the official policy or position of the Department of Defense or the U.S. Government.

tracking NEAs. SST uses the same detection software that the LINEAR program does, which does not utilize a "master image" of the sky for image differencing, but benefits from the much larger aperture to obtain significantly better performance for detecting dim objects in space. This makes SST the most recent U.S. space surveillance system to join the search for NEAs, and if its performance can be improved a greater percentage of NEAs will be found.

The mission requirements for SST differ from typical astronomical telescopes. SST is designed to scan deep space to detect and correlate unknown space objects rather than dwell on stellar objects over relatively long periods of time (Monet et al. 2012). In this sense, SST is a precursor to other wide field of view (FOV) synoptic search programs like LSST. These programs are funded by NASA to provide full sky coverage with frequent revisit times in hopes of finding and cataloging NEAs. SST is expected to provide initial detections of asteroids for follow-up by other more detailed scientific instruments for cataloging by NASA.

Currently SST uses an algorithm developed from a binary hypothesis test (BHT) to detect space objects in a single image for use by the LINEAR program (Viggh et al. 1998). The two hypotheses are the null hypothesis that a space object's image is not in a pixel (H_0) and the alternative hypothesis that the image is in a pixel (H_1). Positive detection decisions in three successive frames are then used to build a track that is then used to help predict the future position of the object. If an object does not appear in three successive frames, it is rejected. This helps eliminate non-Gaussian sources of noise, such as cosmic rays or data communication errors from the photo-detector. When the telescope tracks at the sidereal rate, nearby space objects naturally move across the CCD array. In this way, all objects outside the solar system appear to be stationary, whereas objects within the solar system will appear in different pixels at different times, based on their trajectory and the time between the frames in which they are observed.

In contrast to a BHT, we propose a multi-hypothesis testing (MHT) for single frame detection that selects from the hypotheses that the image is in the center, a corner, or a side of a pixel (H_1–H_9) in addition to H_0. Although the use of more hypotheses might increase the detection performance of this scheme, a finite number of hypotheses must be chosen in order to make using the test numerically tractable. The results obtained using nine alternative positional hypotheses serve to demonstrate the utility of the MHT over a BHT, but do not necessarily represent the optimal performance achievable by an MHT. Both of these tests consider the noise to be Gaussian. Another method of BHT developed by Pohlig, however, has been derived using a Poison noise distribution, which is not used for comparison in this study because the SST sensor is dominated by readout noise rather than shot noise a low light levels (Pohlig 1989).

The experiment conducted as part of this research is designed to determine which type of algorithm is best at detecting dim unresolvable objects in space on a single frame basis. Because single frame detection decisions are typically used as input to multi-frame detection and tracking algorithms, a superior single frame detector will enhance the performance of any synoptic search telescope looking for NEAs or space debris using this three-frame coincidence approach (Viggh et al. 1998). In order to perform this study, we chose to observe a satellite in a geosynchronous orbit that is gradually going into eclipse behind the earth. In this scenario, the unresolvable satellite body experiences an ever-decreasing amount of solar illumination, which provides a continuum of intensity values over which to test the performance of different algorithms. The presence and location of the satellite is simple to establish when it is brightly lit, so all detection algorithms will successfully detect the object before it begins to go into eclipse. The telescope is pointed directly at the satellite and then observes it as it goes into the shadow of the earth. Because the presence of the object is known (and further verified when it emerges from the eclipse) the performance of the different detection algorithms can be ascertained in a controlled environment. Also, because the object is in geosynchronous orbit, it stays relatively stationary in the sky, and thus the object requires practically no tracking motion from the telescope motors. With the object location relatively fixed, different detection algorithms are tested using the observations of the dimming satellite. The detection algorithm that successfully reports the presence most consistently through the eclipse period is clearly superior. This method of testing detection algorithms is preferable to performing algorithm tests against unknown objects that may or may not actually exist. This also precludes the possibility of making a firm conclusion as to which algorithm is actually detecting an object with a higher success rate versus a detector that produces more false detections.

Two types of BHTs are compared with the MHT, one is the baseline point detector used by SST and the other is a matched-filter technique (i.e., correlation detector) similar to that used by the Pan-STARRS program (http://Pan-STARRS.ifa.hawaii.edu/public/). The advantage of an MHT is gained in part by mitigating the aliasing caused by the undersampled SST images (O'Dell & Cain 2009). The equations for both the BHT and MHT are derived in terms of signal-to-noise ratio (S/N; Viggh et al. 1998; Kay 2011). The hypothesis that maximizes S/N while simultaneously increasing the probability of detection (P_d) is chosen thereby providing sub-pixel position information on the image location and increasing P_d over the BHTs.

The comparison of the different hypothesis testing methods on the basis of probability of detection and processing requirements is made using data collected from the experiment described in the next section. A modeled point-spread function (PSF) is generated using the phase retrieval technique presented in Section 4 and then it is dithered to facilitate the creation of the MHT. This PSF model is utilized because it has been proven and documented to work with SST in the past (Woods 2012). In Section 5 a comparison of an MHT to the BHTs is conducted to illustrate the advantages of the MHT as well as its additional computational burden. At the conclusion of Section 5, a derivation shows that the S/N results of the MHT are linearly related to the least-squares (LS) estimates of point source irradiance, which improves photometry.

2. SST EXPERIMENTAL DESCRIPTION

As stated in the introduction, the purpose of this experiment is not to find a new object in space using SST, but to instead run different detection algorithms on data containing a very dim, but known object so that the relative performance of different detection algorithms can be compared in a controlled environment. The experimental method provides a data set that is used to form a clearly supportable conclusion as to what algorithm should be used to help detect dim objects in space from single frame measurements. In essence, it is not possible to measure the probability of detection for a system without knowing with certainty that an object is present to detect. In addition to the experimental description, a basic overview of the SST's design and current detection strategy are covered.

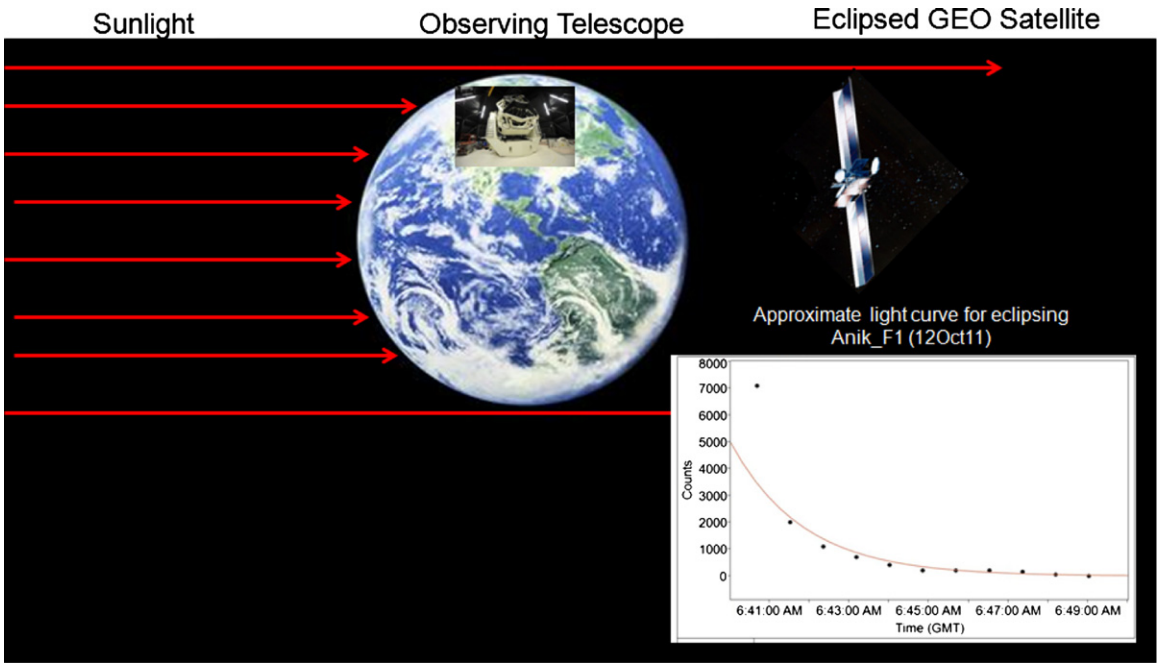

Figure 1. Eclipse experiment overview (Vollmer & Gedzelman 2008; Verba et al. 2009; see also http://www.boeing.com).

2.1. Experimental Setup and Process Overview

The experiment was conducted by imaging a GEO communications satellite, ANIK-F1, with SST in a test mode as the satellite went into eclipse during the 2012 vernal equinox over a period of about 4 minutes, as illustrated in Figure 1.

There are many cataloged dim astronomical objects that could be used to compare detection algorithm performance. By imaging eclipsing GEO satellites, the experimental observations capture both the effect of the irradiance division across pixels that arises from objects moving across the FOV of the telescope, and the decreasing irradiance levels of the satellites as they enter into eclipse. The irradiance levels decrease as the satellites move through the penumbra and into the umbra as illustrated by the light curve produced from data on ANIK-F1 using the U.S. Naval Observatory's (USNO) 1 m telescope and plotted in the lower right hand corner of Figure 1. The roll off of ANIK-F1's irradiance during eclipse was first documented in a series of experiments conducted by USNO to record the glint of GEO satellites shortly before the eclipse (Verba et al. 2009).

The first stage in the experiment is the collection of the raw data. On each night, experiment images of the night sky containing ANIK-F1 were collected using 100 ms exposures a rate of 8 frames per second. The telescope was pointed so that ANIK-F1 was centered in the FOV near the time right before the eclipse. The orbital elements of the satellite were entered into SST's tracking system, so that SST could be programmed to follow the satellite through the eclipse. This required very little tracking movement from the motors as the object in GEO orbit appears to hang in the sky at approximately the same position throughout the data collection. As predicted on many nights of the eclipse, the satellite became too dim to detect with SST's existing detection software (described in the next section). Once the data was collected it was recorded and given to the algorithm test team at AFIT for post-processing.

The next step was the pre-processing phase. The raw SST image data, which is 6144 by 4096 pixels, was reduced to a more manageable data set involving only 200 by 200 pixels around ANIK-F1. This allowed for more efficient use of memory resources within the computer, but still provided a sufficiently large FOV to be certain the satellite was fully contained in the reduced frame and to also capture nearby stars for use in determining the system PSF. At the beginning of the test, ANIK-F1 is bright (roughly a magnitude nine object, which saturates the photo-detectors) and clearly visible in the center of the telescope's FOV. Efforts to manually identify its position are further aided by the fact that it does not change position appreciably throughout the test. Also, the satellite is readily identifiable when it emerges from the eclipse (again returning to its pre-eclipse magnitude), thus a linear trajectory of the object can be predicted through the eclipse and its exact position (to within a pixel) can be predicted for every frame (no other image registration algorithm is required). *A priori* sub-pixel location information is not required to perform the experiment, as all existing tests are designed to make a simple binary decision of whether or not the object is within the pixel.

The next step is to extract the PSF from the images for use by the different detectors. Three different detectors are used to process the data from this test for comparison. The first is the point detector (described in the next section), which is currently used by SST, LINEAR, Pan-STARRS, and other deep space object detection programs (http://Pan-STARRS.ifa.hawaii.edu/public/; Pearce et al. 2003). This detector does not utilize a PSF because it just analyzes the data within a single pixel to make detection decisions. The second detector is the correlator or matched filter detector. This detector is used optionally by the Pan-STARRS program to make detection decisions and requires the use of a PSF (http://Pan-STARRS.ifa.hawaii.edu/public/). As shown in Figure 4, a star is selected to provide the PSF shape for the correlator on each night. The selected star is chosen to match the shape of the satellite observed near the start of the test in order to help maximize the performance of the correlator. The correlator, as implemented by the Pan-STARRS program, is not designed to consider under sampling or sub-pixel motion, so a single empirically measured PSF is used each night to implement this particular detector.

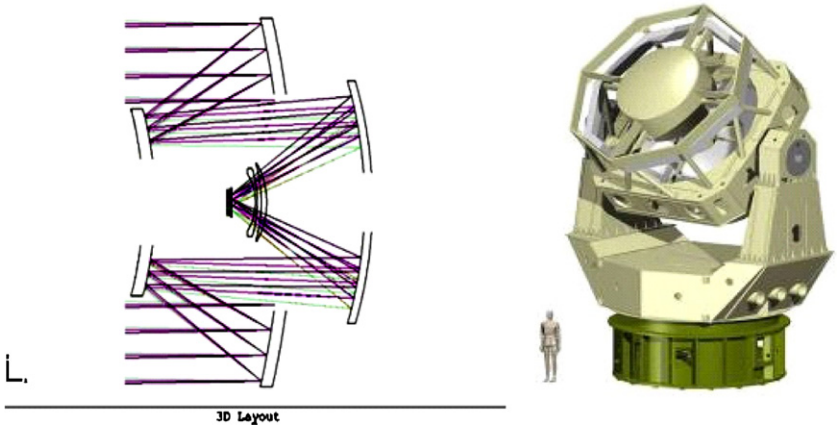

Figure 2. SST 3D layout and scale picture.
(A color version of this figure is available in the online journal.)

The PSF model used for the MHT requires a properly sampled PSF that can be used to generate the PSF shape for the nine different hypotheses used in the test, corresponding to the nine different sub-pixel locations. This was done using a model-based approach. This same optical model was used by the MIT Lincoln labs team just preceding the eclipse event, to measure the PSF to focus and align the telescope in 2012 March. We use the same optical model in hopes of leveraging their experience with the telescope to compute the PSF (Woods 2012). Although other methods for computing a properly sampled PSF from undersampled imagery exist, performing a comparison study between these methods was beyond the scope of this paper (Schödel 2010; Thurman & Fienup 2009; Pinheiro da Silva et al. 2006; Anderson & King 2006, 2000; Lauer 1999). Clearly, a better PSF estimate would lead to even better performance for the MHT method, as it is the only detector tested in this study that utilized a properly sampled PSF. The detailed steps on how the modeled PSF used to construct the MHT is computed are described in Section 4 of this paper.

The final step in the test is to provide each detector with the raw image data in a 19 by 19 window centered on the pixel containing the satellite for all frames of data gathered by SST. Each detector reports an S/N for the satellite for each frame of data. The S/N values over 10 frames are locally averaged to reduce the effect of noise. The averaged S/N is then converted to a probability of detection for the point detector, the correlator, and the MHT using Equations (38)–(40), respectively. Although a detection decision could be made based on the reported S/N for the detector in each frame, the computed probability of detection reflects the statistical chance of making a correct detection decision for the object based on the average S/N and the estimated noise level present in the data. The computed probability of detection is a superior performance metric to S/N or simple detections because it conveys the improvement of one detector over another in terms that can be more readily understood. The results of the reported probability of detection for each detector on each night are reported in Section 6 of this paper.

2.2. SST System

SST has a Mersenne–Schmidt design, which is selected for both its wide FOV and compactness (Willstrop 1984). A three-dimensional (3D) optical design layout and scale image of the telescope is shown in Figure 2. The 3.5 m diameter primary mirror was built to meet the requirement of detecting small faint objects with relatively short integration times, thereby avoiding streaking of the satellite image across multiple CCD pixels so that the objects are suitably modeled as points sources. Another characteristic of the Mersenne–Schmidt design is a curved focal surface, which allows the SST to better optimize spot size across the FOV and spectral response of the CCD. Consequently, the curved CCD imager and mosaic camera were developed specifically for the telescope (Monet et al. 2012).

2.3. SST Detection Process

SST's current detection method is based on the algorithm used for LINEAR conducted at the experimental test site near Socorro, NM. Viggh et al. (1998) described the LINEAR detection algorithm using the block diagram shown in Figure 3.

In normal operating mode the CCD's 15 μm pixels are 2×2 binned and the array has a 6144×4096 binned format. Single frame point detection of an object from SST imagery data, $d(c_x, c_y)$, in a pixel with coordinates (c_x, c_y) is performed in a process of background suppression, normalization, and binary quantization:

$$\mathrm{S/N}(c_x, c_y) = \frac{(d(c_x, c_y) - B)}{\sigma} \underset{H_0}{\overset{H_1}{\gtrless}} \gamma, \tag{1}$$

where B is the local background noise, σ is the standard deviation of the noise, and γ is the detection threshold. The background, B, can be computed as the local sample median of the data in the H_0 case:

$$B = \mathrm{median}[d(w, z)] \tag{2}$$

and the local standard deviation is

$$\sigma = \sqrt{E[d^2(w, z)] - E[d(w, z)]^2} \approx \sqrt{\frac{\sum_{w=1}^{M_d} \sum_{z=1}^{M_d} d^2(w, z)}{M_d^2} - B^2}, \tag{3}$$

where M_d is the number of pixels in one dimension of a chosen window in the CCD array plane centered on the pixel of interest, (c_x, c_y) and $E[]$ represents the expectation operation. Pixels with an S/N greater than the detection threshold are classified as containing a target and passed on for further processing.

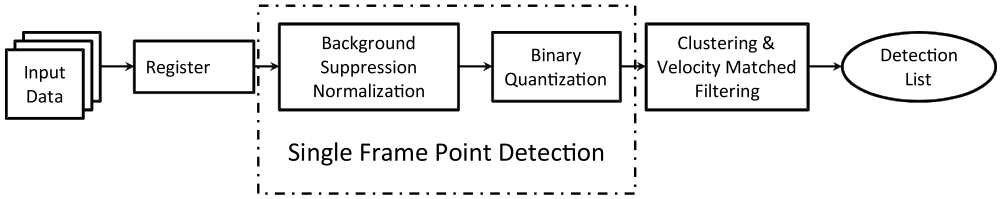

Figure 3. LINEAR detection block diagram. The single frame point detection piece of the system is highlighted in the dotted line box. This piece of the software alone is tested in this paper.

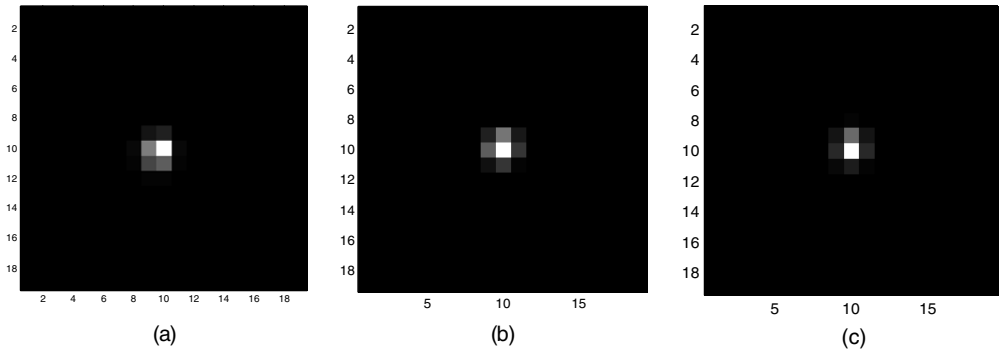

Figure 4. Images of stars used for the correlator on (a) 2012 March 13, (b) 2012 March 14, and (c) 2012 March 15.

3. BINARY HYPOTHESIS TESTING

Replacing the baseline BHT with a correlation-based BHT improves SST's detection performance. This method for improving SST's detection performance is explored by (Maksim et al. 2012) in which a comparison of the S/N of two different BHTs, a correlator and a point detector, is made using the ANIK-F1 experimental data. In this comparison, stars in the FOV are used to estimate the total system PSF. Figures 4(a)–(c) shows the irradiance maps of each star within a 19 × 19 window cropped from SST images on three consecutive nights and used in the correlation detector. One item to note is that in Figures 4(b) and (c) the star appears to have a different shape than the star in Figure 4(a). The change in the apparent shape of the star is due to the images being centered at a different sub-pixel location. If the shape of the object of interest is not the same as the total system PSF used in the correlator, the detection performance will be degraded.

Both the correlator and SST's baseline point detector can be derived from a BHT expressed as the following likelihood ratio tests (LRTs; Kay 2011):

$$\Lambda = \frac{P(d(x,y)\forall(x,y)\in[1,M_d]|H_1)}{P(d(x,y)\forall(x,y)\in[1,M_d]|H_0)} \underset{H_0}{\overset{H_1}{\gtrless}} 1, \quad (4)$$

where $d(x, y)$ is the image data, x and y are the pixel coordinates, and M_d is the number of pixels in one dimension of a chosen square window in the CCD array plane. In this case, H_1 is the hypothesis that an object is present in the pixel of interest and H_0 is the hypothesis that an object is not present in the pixel of interest. $P(d(x, y)\forall(x, y) \in [1, M_d]|H_i)$ is the joint conditional probability of the data, given that hypothesis $H_i, i \in \{0, 1\}$ is true.

The correlator is designed to achieve a chosen probability of false alarm, (P_{FA}), under the H_0 case by approximating the image noise as Gaussian. This is a valid assumption because in the H_0 case, the pixels have a higher proportion of read noise than photon noise. If the detector was designed for the H_1 case, a Poisson distribution for noise would be a better choice; however Pohlig's derivation using that assumption led to a detector that was dependent on target irradiance (Pohlig 1989). To remove the detectors' dependence on target irradiance, a log approximation is made assuming that the target irradiance is low. Thus the distribution of the noise for these dim objects would not be Poisson, but would have a similar distribution. Instead, using a Gaussian noise distribution the LRT becomes

$$\Lambda_G = \frac{P[d(x,y)|H_1]}{P[d(x,y)|H_0]} = \frac{\prod_{w=1}^{M_d}\prod_{z=1}^{M_d}\frac{1}{\sqrt{2\pi}\sigma}e^{\{-\frac{1}{2\sigma^2}[d(w,z)-B-\theta h(w,z)]^2\}}}{\prod_{w=1}^{M_d}\prod_{z=1}^{M_d}\frac{1}{\sqrt{2\pi}\sigma}e^{\{-\frac{1}{2\sigma^2}[d(w,z)-B]^2\}}} \underset{H_0}{\overset{H_1}{\gtrless}} 1, \quad (5)$$

where w and z are pixel locations in the window, and the total system PSF is $h(w, z)$. The value M_d is the total number of pixels in the window, B is the background photo count in the image, θ is the space objects irradiance, and σ is the standard deviation of the noise. The equation for the LRT is designed to maintain the same false alarm rate as the baseline detector that is determined by the H_0 case. Taking the natural log, Equation (5) reduces to the following form:

$$\log(\Lambda_G) = \sum_{w=1}^{M_d}\sum_{z=1}^{M_d}\frac{1}{2\sigma^2}[-2B\cdot\theta h(w,z)+2d(w,z)\cdot\theta h(w,z)-(\theta h(w,z))^2] \underset{H_0}{\overset{H_1}{\gtrless}} 0. \quad (6)$$

Since the PSF can be estimated independently from auxiliary processes, Equation (6) can be rearranged as

$$\sum_{w=1}^{M_d}\sum_{z=1}^{M_d}(d(w,z)-B)h(w,z) \underset{H_0}{\overset{H_1}{\gtrless}} \frac{\theta}{2}\sum_{w=1}^{M_d}\sum_{z=1}^{M_d}[(h(w,z))^2], \quad (7)$$

and the selection of θ will be chosen to achieve the desired threshold. To convert Equation (7) into an equation in terms of

S/N, where S/N is defined as the ratio of the mean divided by the standard deviation, the background suppressed data is a new random variable, d_2, with zero mean in the H_0 case (Goodman 1985):

$$d_2(w,z) = d(w,z) - B. \tag{8}$$

The correlation of the PSF with the background suppressed data then becomes

$$\sum_{w=1}^{M_d}\sum_{z=1}^{M_d} d_2(w,z)h(w-c_x, z-c_y), \tag{9}$$

where c_x and c_y are the coordinates of the pixel being tested. The resulting quantity also has a mean, $\mu_{2,}$ where

$$\begin{aligned}\mu_2 &= \mathrm{E}\left[\sum_{w=1}^{M_d}\sum_{z=1}^{M_d} d_2(w,z)h(w-c_x, z-c_y)\right] \\ &= \sum_{w=1}^{M_d}\sum_{z=1}^{M_d} E[d_2(w,z)]E[h(w-c_x, z-c_y)] = 0,\end{aligned} \tag{10}$$

and the variance, σ_2^2, of

$$\begin{aligned}\sigma_2^2 &= E\left[\left(\sum_{w=1}^{M_d}\sum_{z=1}^{M_d} d_2(w,z)h(w-c_x, z-c_y)\right)^2\right] \\ &= E\left[\sum_{w=1}^{M_d}\sum_{z=1}^{M_d} d_2(w,z)h(w-c_x, z-c_y)\right. \\ &\quad \left.\times \sum_{m=1}^{M_d}\sum_{n=1}^{M_d} d_2(m,n)h(m-c_x, n-c_y)\right] \\ &= \sum_{w=1}^{M_d}\sum_{z=1}^{M_d}\sum_{m=1}^{M_d}\sum_{n=1}^{M_d} E[d_2(w,z)]E[d_2(m,n)] \\ &\quad \times h(w-c_x, z-c_y)h(m-c_x, n-c_y).\end{aligned} \tag{11}$$

Equation (11) can be solved using two cases, one when $w \neq m$ and $z \neq n$, and the other when $w = m$ and $z = n$ using the Dirac delta function, $\delta(w-m,\ z-n)$, such that

$$\begin{aligned}\sigma_2^2 &= \sum_{w=1}^{M_d}\sum_{z=1}^{M_d}\sum_{m=1}^{M_d}\sum_{n=1}^{M_d} E[d_2(w,z)]E[d_2(m,n)] \\ &\quad \times h(w-c_x, z-c_y)h(m-c_x, n-c_y) \\ &\quad \times (1-\delta(w-m, z-n)) \\ &\quad + \sum_{w=1}^{M_d}\sum_{z=1}^{M_d} E\left[d_2^2(w,z)\right]h^2(w-c_x, z-c_y) \\ &\quad \times \delta(w-m, z-n) \\ &= \sigma^2 \sum_{w=1}^{M_d}\sum_{z=1}^{M_d} h^2(w,z).\end{aligned} \tag{12}$$

Therefore, the standard deviation of the normalized data correlated with the total system PSF is

$$\sigma_2 = \sigma\sqrt{\sum_{w=1}^{M_d}\sum_{z=1}^{M_d} h^2(w,z)}. \tag{13}$$

The equation for the correlator is then found by dividing Equation (7) by Equation (13), such that the LRT reduces to the following correlation operation normalized in terms of S/N:

$$\begin{aligned}\mathrm{S/N_{corr}} &= \frac{\sum_{w=1}^{M_d}\sum_{z=1}^{M_d}(d(w,z)-B)h_{\mathrm{corr}}(w-c_x, z-c_y)}{\sigma\sqrt{\sum_{w=1}^{M_d}\sum_{z=1}^{M_d} h_{\mathrm{corr}}^2(w,z)}} \underset{H_0}{\overset{H_1}{\gtrless}} \\ &\quad \times \frac{\frac{\theta}{2}\sum_{w=1}^{M_d}\sum_{z=1}^{M_d}[(h(w,z))^2]}{\sigma\sqrt{\sum_{w=1}^{M_d}\sum_{z=1}^{M_d} h_{\mathrm{corr}}^2(w,z)}} = \gamma,\end{aligned} \tag{14}$$

where the correlator PSF $h_{\mathrm{corr}}(w,z)$ is approximated using the intensity values of the cropped stars shown in Figure 4. The results of the equation are then compared against the selected S/N threshold, γ, which is set to achieve a desired P_{FA}.

In the case of the baseline point detector, the PSF is one pixel represented as a delta function, $\delta(w-c_x, z-c_y)$. The equation for the baseline detector in terms of S/N is

$$\begin{aligned}\mathrm{S/N_{Baseline}} &= \frac{\sum_{w=1}^{M_d}\sum_{z=1}^{M_d}(d(w,z)-B)\delta(w-c_x, z-c_y)}{\sigma\sqrt{\sum_{w=1}^{M_d}\sum_{z=1}^{M_d}\delta^2(w,z)}} \\ &= \frac{(d(c_x,c_y)-B)}{\sigma} \underset{H_0}{\overset{H_1}{\gtrless}} \gamma\end{aligned} \tag{15}$$

and thus can be compared against the same threshold as the correlator.

SST's threshold used for detection during the technical demonstration period is $\gamma = 6$, which inherently sets the probability of false alarm. The probability of false alarm is defined as the chance that a pixel that contains only background light (no object) will produce a detector output that exceeds the threshold value of six. When objects are not present in the pixel, the operations described in Equations (14) and (15) are designed to produce unit variance zero mean Gaussian random variables, therefore the probability of false alarms per pixel (ignoring non-Gaussian forms of noise) is

$$\begin{aligned}P_{\mathrm{FA}} &= P(\mathrm{S/N_{Baseline}} \geqslant 6|H_0) = P(\mathrm{S/N_{corr}} \geqslant 6|H_0) \\ &= \int_6^\infty \frac{1}{\sqrt{2\pi}} e^{\frac{-t^2}{2}} dt = 9.87\mathrm{e}-010.\end{aligned} \tag{16}$$

4. SST PSF MODELING

A modeled PSF is used for characterizing SST's impulse response in this paper, because previous efforts to focus and align the telescope's optics used this model successfully (Woods 2012). Although other methods exist for characterizing a PSF from undersampled data (Anderson & King 2006; Lauer 1999), determining which PSF characterization method is superior is not the focus of this research. The telescope optics are modeled as a linear shift invariant system, where the impulse response of the system is the optical PSF. Light propagating from the distance point source (i.e., a star) is assumed to be temporally incoherent. Therefore, according to Goodman, the image irradiance, $i(x)$, in the CCD array plane coordinates, x, of the continuous image is the convolution of point source irradiance, $\delta(x)$, with the telescope's PSF, $h_{\mathrm{opt}}(x)$ (Goodman 2005).

The pupil function, $A(u,v)$, of the telescope is defined by its annular aperture, where u and v are coordinates in the pupil plane. Wave front errors caused by telescope aberrations are

introduced into the pupil function using the first N Zernike polynomials, $\phi_2 - \phi_N$, where N is the maximum number of polynomials (Noll 1976). The amount of wave front error is captured by scaling the Zernike polynomials with the Zernike coefficient, $Z_2 - Z_N$,

$$\text{error}(u, v) = Z_2\phi_2(u, v) + \cdots + Z_N\phi_N(u, v). \quad (17)$$

Compressing the notation from two dimensions to one dimension for simplified presentation, the aberrations are then represented in the pupil plane coordinates, u_1, by the generalized pupil function

$$\mathsf{P}(u_1) = A(u_1)\exp[j \cdot \text{error}(u_1)]. \quad (18)$$

The incoherent PSF is then computed by propagating the pupil field using Franhofer propagation to the CCD array and then taking the magnitude squared (Goodman 2005),

$$h_{\text{opt}}(x) = \left| \int \mathsf{P}(u_1) e^{\frac{j2\pi x u_1}{\bar{\lambda} \cdot z}} du_1 \right|^2, \quad (19)$$

where z is the distance from the pupil plane to the image plane. The telescope's optical transfer function, $\mathsf{H}_{\text{opt}}(u_1)$, is computed using a Fourier transform, F,

$$\mathsf{H}_{\text{opt}}(u_1) = \mathsf{F}\{h_{\text{opt}}(x)\}. \quad (20)$$

The effect of the finite square pixels, $a = 30\ \mu$m, is determined using a rectangle function with the following transfer function:

$$\mathsf{H}_{\text{pixel}}(u_1) = \mathsf{F}\{rect(ax)\}. \quad (21)$$

Because SST uses a shutter, with an integration time greater than 25 ms, an accepted model for that atmosphere is a long-exposure atmospheric transfer function (Goodman 1985):

$$\mathsf{H}_{\text{atm}}(u_1) = \exp\left\{-3.44\left(\frac{\bar{\lambda} \cdot z \cdot u_1}{r_0}\right)^{5/3}\right\}. \quad (22)$$

In this equation r_0 is the atmospheric seeing parameter. The modeled PSF centered on a pixel is then computed as

$$h_{\text{model}}(x) = \mathsf{F}^{-1}\{\mathsf{H}_{\text{opt}}(u_1)\mathsf{H}_{\text{pixel}}(u_1)\mathsf{H}_{\text{atm}}(u_1)\}. \quad (23)$$

One important property of the Nyquist sampled PSF is that a sub-pixel shift, Δx, of the model does not change its shape. Modeling the effects of Δx on the image irradiance pattern is necessary because the point source is not always in the center of the pixel. To reproduce the change in the irradiance pattern measured by each of the 30 μm pixels in the CCD as a function of Δx, the modeled PSF is down-sampled using the ratio L between the 30 μm pixels and the Nyquist pixel size from Equation (19). The shifted and down-sampled PSF is

$$h_{\text{samp}}(m, \Delta x) = \int h_{\text{model}}(x)\delta(Lm - x - L\Delta x)dx, \quad \text{and} \quad (24)$$

thus the sampled irradiance is

$$i_{\text{samp}}(m, \Delta x) = \theta h_{\text{samp}}(m, \Delta x) + B, \quad (25)$$

where B is the background light, θ is the total number photons emitted from the object per integration, and m is a integer valued pixel location in the CCD array.

To build the PSF model, estimates of the coefficients Z_5–Z_{11} were made using the DONUT algorithm and inserted into the PSF model using Equation (17) (Woods 2012). Then, the method of LS is used to jointly estimate the Zernike coefficient for defocus, $\hat{Z}_4$, and the atmospheric seeing parameter, $\hat{r}_0$, from a star selected from the first frame in the ANIK F1 experimental data (see Figure 4). $\hat{Z}_4$ and $\hat{r}_0$ are estimated using phase retrieval, because seeing changes as a function of time, and focus changes as a function of telescope elevation and temperature, therefore neither parameter is static. For phase retrieval, the sampled image irradiance model in Equation (25) is varied to define elements in the sum of the squares matrix, Q_{ij}, used for LS method:

$$Q_{ij} = \sum_m (d(m) - i_{\text{samp}}(m, \Delta x))^2, \quad (26)$$

where $d(m)$ are the data from a star and the indices i and j correspond to a grid of possible r_0 and Z_4 values used to form $h_{\text{samp}}(m, \Delta x)$. To accurately represent the $i_{\text{samp}}(m, \Delta x)$ that is used in defining the sum of squares matrix, $\underline{\underline{Q}}$, an estimate of the object's irradiance, $\hat{\theta}$,must be determined from the data by taking the derivative of Equation (26) with respect to θ, setting it equal to zero, and solving for the estimate $\hat{\theta}$,

$$\hat{\theta} = \frac{\sum_m [d(m) - B]h_{\text{samp}}(m, \Delta x)}{\sum_m h^2_{\text{samp}}(m, \Delta x)}. \quad (27)$$

The joint estimate for defocus and seeing is then found by

$$\begin{bmatrix} \hat{Z}_4 \\ \hat{r}_0 \end{bmatrix} = \underset{Z_4, r_0}{\arg\min} \left(\underline{\underline{Q}}\right). \quad (28)$$

A color map of the PSF model generated using a SST star image on 2012 March 14 with both Nyquist and 30 μm sampling are shown, respectively, in Figures 5(a) and (b). In the SST data, $d(m)$, the star image can be centered at any sub-pixel location and the corresponding irradiance pattern changes. By shifting the modeled PSF, the changes in the irradiance pattern in the star data can be captured. If the PSF is undersampled spatially, as is the case with the 30 μm detected PSF, the shifted PSF will have aliasing artifacts (O'Dell & Cain 2009). Figure 5(c) depicts the aliasing artifacts produced when the undersampled PSF is shifted using the Fourier transform shift method:

$$p_m = \cos(m \cdot \Delta x) + i\sin(m \cdot \Delta x), \quad \text{and} \quad (29)$$

$$h_{\text{shift}}(m, \Delta x) = RE[F^{-1}\{F\{h_{\text{samp}}(m)\}p_m\}], \quad (30)$$

where Δm magnitude of sub-pixel PSF shift such that the modeled irradiance is

$$i_{\text{shift}}(m, \Delta x) = \theta \cdot h_{\text{shift}}(m, \Delta x) + B. \quad (31)$$

However, if the Nyquist sample model is shifted before down sampling to 30 μm using Equation (24), as shown in Figures 5(d) and (e), the irradiance pattern does not have the same aliasing artifacts as seen in Figure 5(c).

The accuracy of the sampled irradiance models shifted two different ways can be quantified using the correlation coefficient (Kutner et al. 2005). The correlation coefficient measures how accurately the modeled irradiance pattern matches the measured irradiance pattern on a scale from zero to one, where a value of one means they are perfectly correlated and zero means

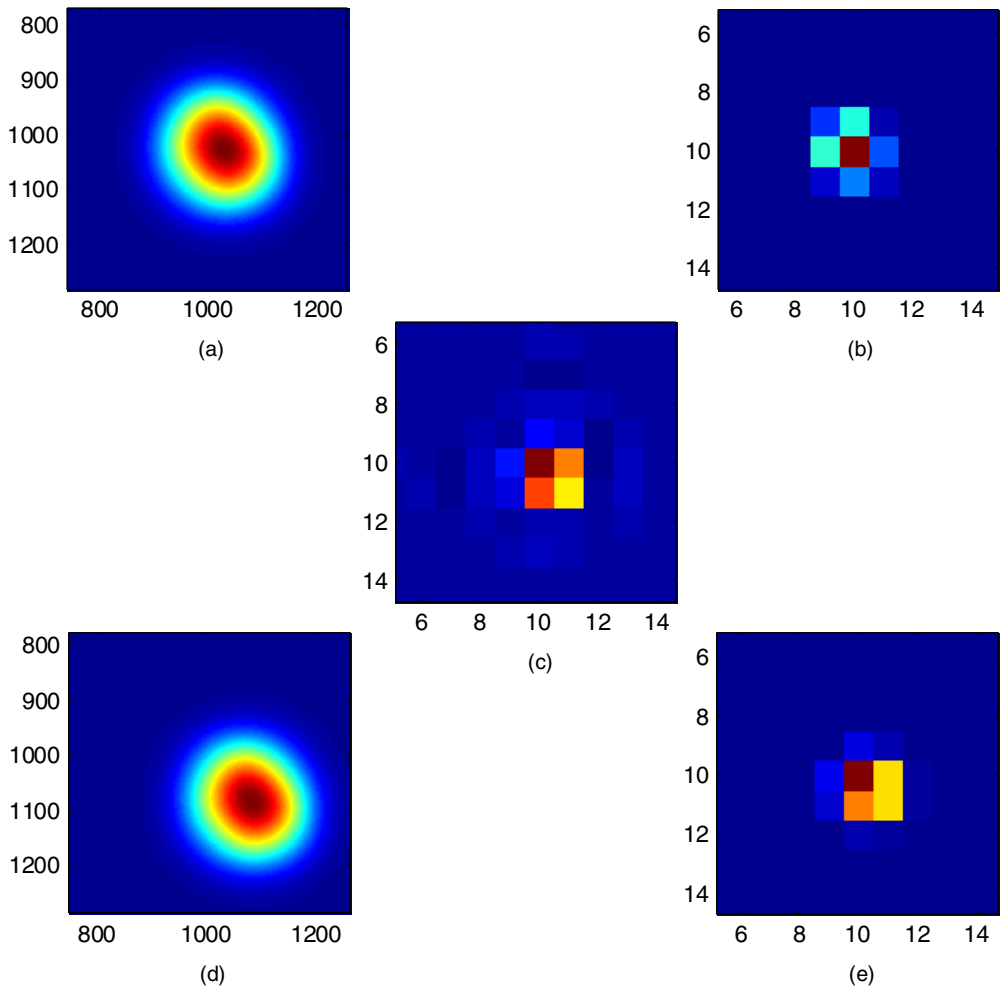

Figure 5. SST's phase retrieved PSF on 2012 March 14. (a) Centered Nyquist sample PSF, $a = 2.75\text{e-}07$ m, on a 2048 × 2048 grid, (b) centered down-sampled PSF, $a = 30\ \mu$m, on a 19 × 19 grid, (c) model PSF, $a = 30\ \mu$m, shifted to the lower right hand corner of pixel (10,10) with aliasing artifacts, (d) Nyquist sample model PSF shifted without aliasing artifacts, and (e) sampled model PSF, $a = 30\ \mu$m, down sampled from Nyquist sampled model PSF shifted to the lower right hand corner of pixel (10,10) without aliasing artifacts.

(A color version of this figure is available in the online journal.)

they are uncorrelated. The correlation coefficient between both irradiance models, Equations (27) and (33), and the measured data are computed, respectively, as

$$\rho_{\text{shift}}(m, \Delta x) = \rho\{d(m), i_{\text{shift}}(m, \Delta x)\} = \frac{E[(d(m) - B)(\hat{\theta} \cdot h_{\text{shift}}(m, \Delta x))]}{\sqrt{E[(d(m) - B)^2]}\sqrt{E[(\hat{\theta} \cdot h_{\text{shift}}(m, \Delta x))^2]}} \tag{32}$$

and,

$$\rho_{\text{samp}}(m, \Delta x) = \rho\{d(m), i_{\text{samp}}(m, \Delta x)\} = \frac{E[(d(m) - B)(\hat{\theta} \cdot h_{\text{samp}}(m, \Delta x))]}{\sqrt{E[(d(m) - B)^2]}\sqrt{E[(\hat{\theta} \cdot h_{\text{samp}}(m, \Delta x))^2]}}. \tag{33}$$

Figure 6 is a plot of the maximum values of $\rho_{\text{shift}}(m, \Delta x)$ and $\rho_{\text{samp}}(m, \Delta x)$ for images of ANIK-F1 on 2012 March 14 as its irradiance is split between pixels. As ANIK-F1's irradiance moves

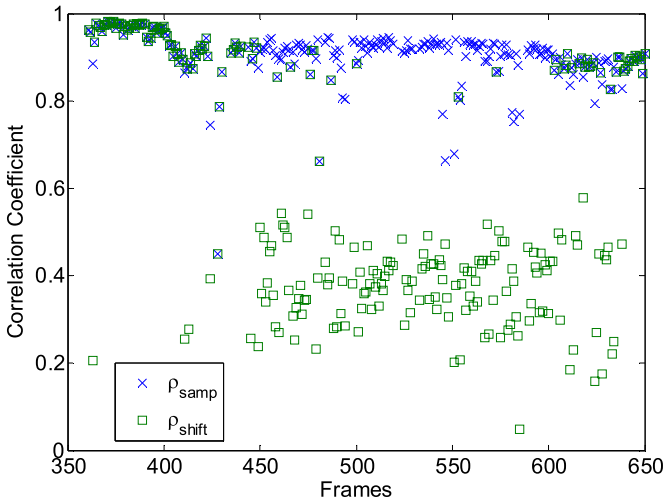

Figure 6. Correlation between two different irradiance models and the images of ANIK-F1 on 2012 March 14 as its irradiance is split between pixels. One model is shifted on the undersampled grid, $\rho_{\text{shift}}(m, \Delta x)$, and the other on a Nyquist grid and then down sampled, $\rho_{\text{samp}}(m, \Delta x)$.

(A color version of this figure is available in the online journal.)

between pixels, even though $i_{\text{shift}}(m, \Delta x)$ is shifted to maximize the correlation coefficient, the $\rho_{\text{shift}}(m, \Delta x)$ goes down. By contrast, the maximum value of $\rho_{\text{samp}}(m, \Delta x)$ is relatively constant regardless of where in the pixel the irradiance of ANIK-F1 is located, thus illustrating the importance generating a Nyquist sampled model. In addition, the strong correlation between the modeled PSF and the data indicates that the model is an accurate representation of the SST PSF.

5. DATA NORMALIZATION USING OUTLIER REJECTION TECHNIQUES

Another feature of the proposed algorithm design is that background noise statistics are computed using a reduced set of data from the window around the pixel to be tested. This new noise power estimation technique rejects any noise sample in the window surrounding the pixel to be tested, if its values do not conform to those predicted by Gaussian statistics. In this way, bad pixels and nearby stars are not used to compute the noise generated by the background light. Current algorithms used by SST and LINEAR use all the pixels in the window surrounding the point to be tested to compute the local noise standard deviation, σ (Viggh et al. 1998). In this process, the background, B, is computed as in Equation (2). The squared deviations, D, from the background within the window are computed as

$$D(m) = (d(m) - B)^2. \tag{34}$$

These squared deviations follow a chi-Squared distribution based on the assumed Gaussian nature of the data, d. The mean of the squared deviations, M, within the window is found as

$$M = E[D(m)], \tag{35}$$

then the standard deviation, S, of D is computed:

$$S = \sqrt{E[D^2(m)] - E[D(m)]^2} \approx \sqrt{\frac{\sum_{m=1}^{M_d} D^2(m)}{M_d^2} - M^2}. \tag{36}$$

A new noise standard deviation ζ, is computed from the window using Equation (3) by excluding any pixel, m, in the calculation where $D(m) \geqslant (M + 3 \cdot S)$. The new noise standard deviation is included in the following MHT for improved detection performance by normalizing the data as in Equation (1) by replacing σ with ζ.

6. MULTI-HYPOTHESIS TESTING

A multi-hypothesis detector is introduced because the image of a space object does not always fall in the center of the pixel. In addition, simple correlation operations are not desirable because the shape of the sampled PSF changes depending on where the object is imaged on the array. In order to account for the possibility that the image is in different places within the CCD array, we introduce a multi-hypothesis test strategy. The hypothesis that an image of a space object is not present in the pixel, H_0, plus the nine different sampled PSF shapes chosen for this example based on the sub-pixel location, form the ten hypotheses for the MHT, $\{H_0, H_1, \ldots, H_9\}$, as depicted in Figure 7. This choice of hypotheses captures a great deal of the spatial dependence of the PSF, while only introducing one order of magnitude more computations.

According to Kay (2011), the multi-hypothesis decision to select one hypothesis, H_k over another hypothesis, H_i, based on uniform cost and equal priors using conditional probabilities is the multi-hypothesis maximum likelihood (ML) decision rule:

$$p(x|H_k) > p(x|H_i) \quad i \neq k. \tag{37}$$

Applying the ML decision rule to Equation (15) with the additional hypotheses based on sub-pixel position shifts listed in Table 1, α_a and β_a, becomes

$$\text{S/N}_a = \frac{\sum_w^{M_d}\sum_z^{M_d}(d(w,z)-B)h_{\text{samp}}(w+c_x-\alpha_a, z+c_y-\beta_a)}{\zeta\cdot\sqrt{\sum_w^{M_d}\sum_z^{M_d}h_{\text{samp}}^2(w,z)}} \underset{H_0}{\overset{H_a}{>}} \gamma_{\text{M-ary}}. \tag{38}$$

Table 1
Alternative Hypothesis Sub-pixel Shifts (Corresponding to Figure 7)

Alternative (a)	Horizontal Shift (α_a)	Vertical Shift (β_a)
1	0	0
2	0	$-15\,\mu$m
3	0	$15\,\mu$m
4	$15\,\mu$m	0
5	$-15\,\mu$m	0
6	$15\,\mu$m	$-15\,\mu$m
7	$15\,\mu$m	$15\,\mu$m
8	$-15\,\mu$m	$-15\,\mu$m
9	$-15\,\mu$m	$15\,\mu$m

1. *H_0: hypothesis that no satellite is present.*
2. *H_a: hypothesis that a satellite is present (see Table 1).*

With this approach, the hypothesis that satisfies the ML decision rule given in Equation (37) is determined by finding

$$\text{S/N}_{\text{M-ary}} = \max(\text{S/N}_a), \tag{39}$$

which simultaneously increases the probability of detection and provides sub-pixel image location information.

Testing each pixel for H_0–H_9 repeats the exact same test four times in the corners and two times on the sides when the entire array is processed because the pixels share sides and corners. Therefore, to minimize the number of hypothesis tests, each pixel only needs to be tested in the center, on one corner and on two sides. This brings the computational cost to that of six times the baseline approach, which only does one test per pixel and does not involve a filtering operation to perform the test. The filtering operation increases the computational cost by 50% or 1.5 times over the point detector's computational cost, thus four times as many tests that cost 1.5 times as much brings the cost to six times that of the baseline point detector approach.

An important goal in deriving the MHT is to improve the probability of detection, P_D, without raising the probability of false alarm, P_{FA}. In this case the probability of false alarm is the chance that a pixel with no space object in it will be classified as having one. In mathematical terms, this is the probability that the S/N will exceed the threshold of γ. Computing the false alarm probability is a challenging task and may prove mathematically intractable. Instead, we compute an upper bound on the probability of the false alarm and then use that upper bound as our estimate of the false alarm probability. This guarantees that the new MHT test will not raise the probability of the false alarm over the existing BHT used by SST and LINEAR.

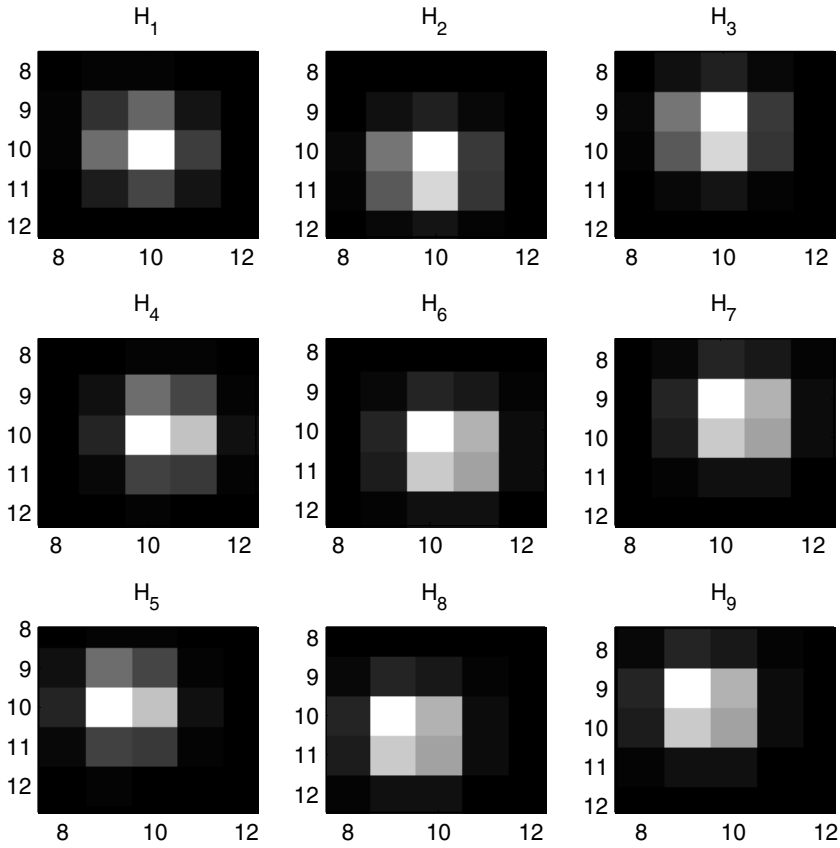

Figure 7. Hypothesis that the image is in either the center of the pixel, H_1; on the sides, H_2–H_5; or the corner of a pixel, H_6–H_9.

Two simplifying assumptions are made to find the upper bound of the $P_{\rm FA}$ for the multi-hypothesis test. The first is considering $P_{\rm FA}$ for each alternative hypothesis to be mutually exclusive, such that $\bigcap_{a=1}^{4} H_a = \emptyset$. The second assumption is that the result of each individual sub multi-hypothesis test is statistically independent of each other. Under those two conditions, the estimated $P_{\rm FA}$ computed for the multi-hypothesis test using only the simple Gaussian noise model (and ignoring other forms of noise) can be bounded above by extending Equation (16) to

$$\begin{aligned} P_{\rm FA} &= P\left(\bigcup_{a=1}^{4} H_a|H_0\right) - P\left(\bigcap_{a=1}^{4} H_a|H_0\right) \\ &\leqslant P\left(\bigcup_{a=1}^{4} H_a|H_0\right) \\ &= \sum_{a=1}^{4} P\left(H_a|H_0\right) = 4 \cdot P\left(\mathrm{S/N}_{M-\mathrm{ary}} \geqslant 6|H_0\right) \\ &\approx 4 \times 9.87\mathrm{e}-010 = 3.94\mathrm{e}-009. \end{aligned} \quad (40)$$

The estimated $P_{\rm FA}$ is higher for the multi-hypothesis test than for the BHT, but it can be reduced by raising the multi-hypothesis detection threshold to S/N = 6.2212, so that $P_{\rm FA}$ = 9.87e-10. This is the estimated single frame probability of the false alarm, using only simple Gaussian noise assumptions. Other spurious forms of noise are assumed to be reduced through the velocity-matched filter, which is a time-domain process that requires the detection of an object in successive frames at locations in the CCD array consistent with an object moving at a fixed velocity.

An example of the detection performance gains from the multi-hypothesis test is shown in Figures 8(a)–(f). To produce the plots, running averages with a 50 frame window for the baseline detector S/N, $\mu_{\rm Baseline}$, the correlator S/N, $\mu_{\rm corr}$, and the multi-hypothesis test S/N,$\mu_{\rm M-ary}$, were found in the threshold region for all three detectors. The probability of detection for the baseline detector, correlator, and multi-hypothesis test as a function of running average are, respectively,

$$P_{D_{\rm Baseline}}(\mu_{\rm Baseline}) = \left(\int_6^{\infty} \frac{1}{\sqrt{2\pi}} e^{\frac{-(t-\mu_{\rm Baseline})^2}{2}} dt\right)^3, \quad (41)$$

$$P_{D_{\rm corr}}(\mu_{\rm corr}) = \left(\int_6^{\infty} \frac{1}{\sqrt{2\pi}} e^{\frac{-(t-\mu_{\rm corr})^2}{2}} dt\right)^3, \quad \text{and} \quad (42)$$

$$P_{D_{\rm M-ary}}(\mu_{\rm M-ary}) = \left(\int_{6.2212}^{\infty} \frac{1}{\sqrt{2\pi}} e^{\frac{-(t-\mu_{\rm M-ary})^2}{2}} dt\right)^3, \quad (43)$$

based on the Gaussian noise assumption and the fact that tracklets require three consecutive frames for detection (Viggh et al. 1998). Note that the threshold in Equation (43) is adjusted to keep the $P_{\rm FA}$ approximately the same for all three detectors.

When ANIK-F1's irradiance is high, all three detectors can detect the satellite, but the satellite dims as it enters eclipse, so the detectors perform differently. Eventually, the satellite becomes so dim that it is undetectable. The area of interest then becomes the detection threshold region. As seen in Figure 8, on all six nights the multi-hypothesis detector detection performance significantly exceeds both the correlator and the baseline detector. This means that the multi-hypothesis test detects much dimmer objects than the baseline algorithms.

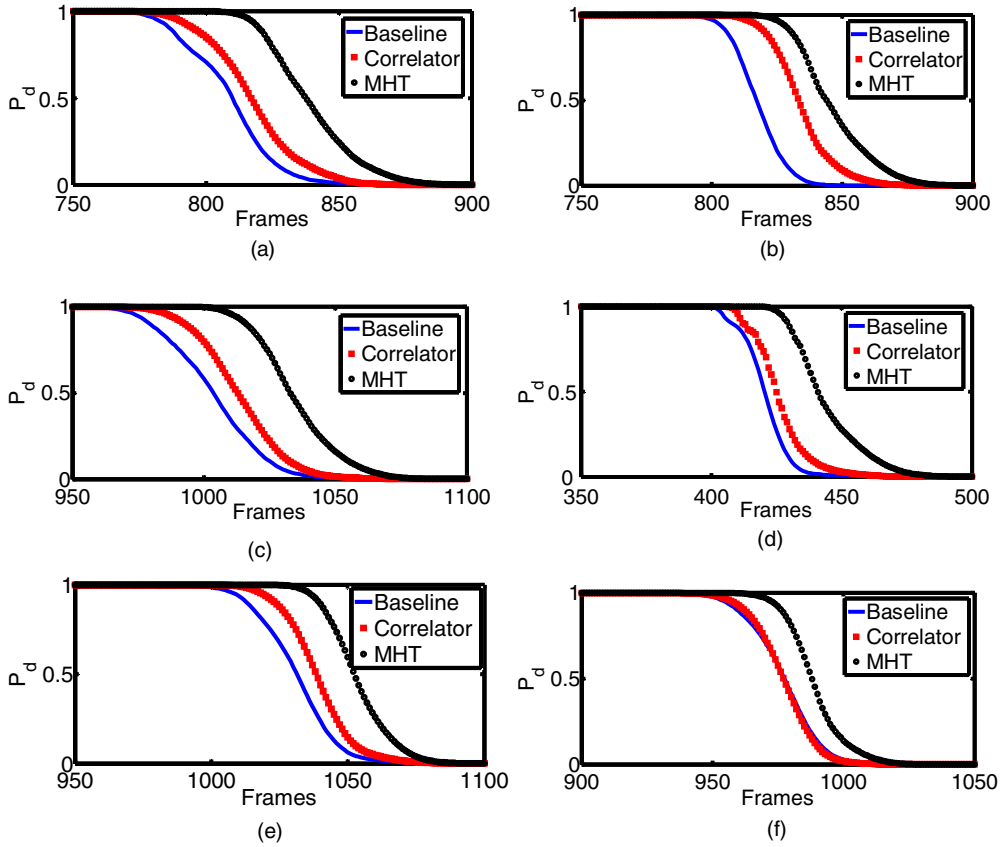

Figure 8. Comparison of the baseline detector, correlator, and multi-hypothesis test probability of detecting (P_d) ANIK-F1 as it enters eclipse on (a) 2012 March 13, (b) 2012 March 14, (c) 2012 March 15, (d) 2012 March 21, (e) 2012 March 22, and (f) 2012 March 23.

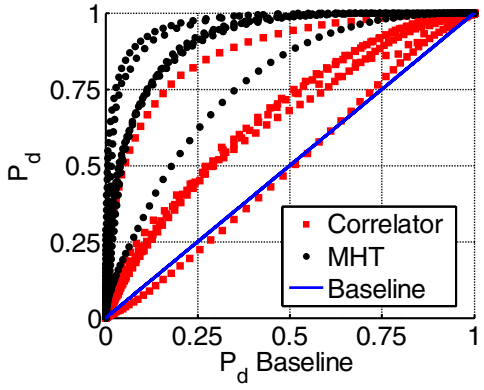

Figure 9. Composite plot of the probability of detecting ANIK-F1 as it enters with either the correlator or multi-hypothesis test vs. the baseline detector for the nights of 2012 March 13–15 and 2012 March 21–23.

The performance gains seen on 2012 March 23 are only due to better calculations of the background noise statistics. On that date there was a narrow total PSF and a lack of aliasing because SST tracked the object in the same pixel.

Using data from six nights of ANIK-F1 eclipse observations, a direct comparison between the baseline detector and both the correlator and multi-hypothesis test shows an improved probability of detecting a space object. A plot of $P_{D_{\rm corr}}(\mu_{\rm corr})$ and $P_{D_{\rm M-ary}}(\mu_{\rm M-ary})$ versus $P_{D_{\rm Baseline}}(\mu_{\rm Baseline})$ for the nights of 2012 March 13–15 and 2012 March 21–23 is shown in Figure 9. The plot shows that the multi-hypothesis test has a higher probability of detection than the correlator and the baseline detector at the detection threshold. On 2012 March 23, the performance gains were not as dramatic because the object's irradiance was concentrated in one pixel due to the satellite's excellent tracking. However, when the object is not is not centered on a pixel, the multi-hypothesis test has a $P_D = 1$ when the baseline has only a $P_{D_{\rm Baseline}} = 0.5$. This 30%–50% demonstrated improvement in the probability of detection means that significantly more dim objects like small asteroids will be found with SST using the multi-hypothesis detector.

In addition to improved detection performance, the multi-hypothesis test can also provide better estimates for object irradiance than the baseline detector. The estimates using the baseline detector are made by adding up the number of digital count in the pixels where the object was detected to estimate the objects' irradiance, $\hat{\theta}_{\rm Baseline}$. In contrast, the S/N output of the multi-hypothesis test is linearly related to the LS estimate of the object's irradiance, $\hat{\theta}_{\rm M-ary}$, in terms of digital counts of by substituting Equation (38) into Equation (27):

$$\hat{\theta}_{\rm M-ary} = \frac{{\rm S/N}_{\rm M-ary} \cdot \sigma}{\sqrt{\sum_m^{M_d} h^2_{\rm samp}(m)}}. \quad (44)$$

Figure 10 shows that by using the multi-hypothesis test results to estimate the object irradiance, a much higher digital count is determined because it is counting information across the 19 × 19 window weighted by the PSF, rather than only the pixels exceeding the threshold. Estimating the digital count more accurately should improve SST's photometric fit results, which have been shown to have a higher variance for objects with magnitudes fainter than 18 M_v (Monet et al. 2012).

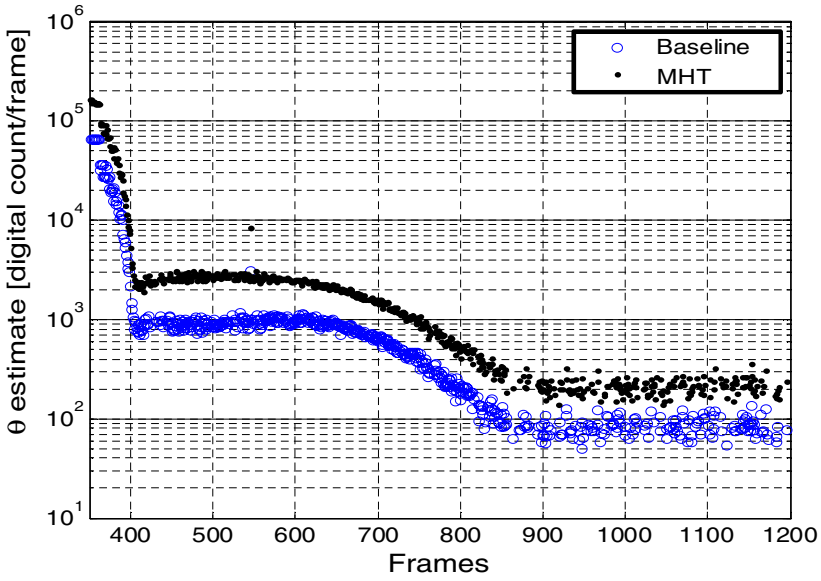

Figure 10. Comparison of the baseline detector and the multi-hypothesis test (least-squares) estimates ANIK-F1 irradiance on 2012 March 14 as it enters eclipse.

7. CONCLUSIONS

The implementation of an MHT by SST will significantly increase the likelihood of achieving the Congressional goal of finding 90% of all asteroids and comets larger than 140 m whose trajectory brings them close to the orbit of Earth (Congress 2005). An MHT can provide a significant improvement in SST's detection capability over a BHT when the object is not centered on a single pixel, as shown in Figure 9. Since SST's mission is to detect unknown space objects, like NEAs, rather than track known objects, it is unlikely that any object will repeatedly fall in the center of a pixel during the three consecutive frames used for detection. The mitigation of the star crossing effects on the noise statistics in the window around the pixel being tested for an object also contributes to the MHT's improved detection performance. These gains are realized by mitigating the aliasing effects of under sampling using a phase retrieved PSF model, but come at the cost of a 600% increase in processing power. Simultaneous to detection, the MHT also provides sub-pixel position information and more accurate estimates of object irradiance. These three improvements to SST's performance by the MHT come with a manageable computational cost that can be afforded with relatively inexpensive modern computers, compared to the cost of enhanced optics, and therefore give good cause to investigate the implementation of this detector.

While the results of this work show that the MHT can provide significant improvement over current BHT methods, more effort should be spent answering the following questions: how does the MHT perform as a function of seeing? How often should phase retrieval be conducted to mitigate seeing effects? How much degradation in performance results from varying changes in PSF? What is the range of PSF shapes that can be tolerated? How much does the performance of the correlation-based BHT depend on the PSF shape? How is the performance of the MHT affected by variations in the PSF across the FOV? Will multiple PSF shapes be used for different positions on the field? If not, what is the degradation in performance if using a single PSF for the field?

One way to investigate the questions about field effects on MHT performance would be to conduct another series of eclipse experiments in which the satellite is imaged in various positions on the CCD known to have different aberrations.

This material is based upon work sponsored by DARPA. In addition, valuable inputs were provided by Deborah Woods and Ronak Shah of MIT Lincoln Laboratories.

REFERENCES

Anderson, J., & King, I. V. 2000, PASP, 112, 1360
Anderson, J., & King, I. R. 2006, Instrument Science Report ACS 2006-01 (NASA: Space Telescope Science Institute)
Congress. 2005, United States 109th Public Law 109–155 (United States Legislation; Washington, DC: United States Government)
Goodman, J. W. 1985, Statistical Optics (New York: Wiley)
Goodman, J. W. 2005, Fourier Optics (Greenwood Village, CO: Roberts and Company)
Gural, P. S., Larsen, J. A., & Gleason, A. E. 2005, AJ, 130, 1951
Kay, S. M. 2011, Fundamentals of Statistical Signal Processing (Upper Saddle River, NJ: Prentice-Hall)
Kutner, M. H., Nachtsheim, C. J., Neter, J., & Li, W. 2005, Applied Linear Statistical Models (New York: McGraw-Hill)
Lauer, T. R. 1999, PASP, 111, 227
LSST Corporation. 2011, Large Synoptic Survey Telescope, Lsst Reference Design. 06 04, http://www.lsst.org/files/docs/overviewV2.0.pdf (accessed 2011 August 14)
Magnier, E. 2007, PSPhot Sofware Design Description, The Pan-STARRS IPP Object Photometry Tool (Honolulu, HI: Univ. Hawaii at Manoa) http://ipp0222.ifa.hawaii.edu/ippData/manuals/psphot.pdf (accessed 2011 August 14)
Maksim, S., Zingarelli, J., & Cain, S. 2012, in Advanced Maui Optical and Space Surveillance Technologies Conference, A Comparison Between a Non-linear, Poisson-based Statistical Detector and a Linear, Gaussian Statistical Detector for Detecting Dim Satellites (Maui, HI: Maui Economic Development Board), 310
Miura, N., & Itagaki, K. 2005, AJ, 130, 1278
Monet, D., Axelrod, T., Blake, T., et al. 2012, AAS Meeting, 221, 352.17
National Aeronautics and Space Administration. 2007, Near-Earth Object Survey and Deflection Analysis of Alternatives Report to Congress (Washington, DC: NASA)
National Aeronautics and Space Administration 2011, NEO Discovery Statistics, http://neo.jpl.nasa.gov/stats/ (accessed 2011 July 26)
Noll, R. 1976, JOSA, 66, 207
O'Dell, A., & Cain, S. 2009, in IEEE Aerospace Conference, Investigating the Effects of Atmospheric Seeing on the Detection of near Earth Orbiting Asteroids, ed. D. Tratt (Big Sky, MT: IEEE), 1527
Pearce, E. C., Shelly, F., & Johnson, J. A. 2003, in Space Control Confrence, High Precision Real Time Processing for the MOSS and LINEAR Systems (Boston: MIT/Lincoln Laboratory)
Pinheiro da Silva, L., Auvergne, M., Toublanc, D., et al. 2006, A&A, 452, 363
Pohlig, S. C. 1989, ITAES, 25, 56
Schödel, R. 2010, A&A, 509, 1

Stokes, G. H., Evans, J. B., & Larson, S. M. 2002, in Asteroids III, Near-Earth Asteroid Search Programs, ed. W. F. Bottke (Tucson, AZ: Univ. Arizona Press), 45
Thurman, S. T., & Fienup, J. R. 2009, JOSAA, 26, 2640
Verba, F. J., Hutter, D., Shankland, P., et al. 2009, in Advanced Maui Optical and Space Surveillance Technologies Conference, A Survey of Geosynchrinous Satellite Glints (Maui, HI: Maui Economic Development Board), 268
Viggh, H. E. M., Stokes, G. H., Shelly, F. C., Blythe, M. S., & Stuart, J. S. 1998, in Proceedings of the 1998 Space Control Conference, Applying Electro-Optical Space Surveillance Technology to Asteroid Search and Detection: The Linear Program Results Lexington, ed. R. G. Galloway & S. Lokaj (Reston, VA: American Society of Civil Engineers), 373
Vollmer, M., & Gedzelman, S. D. 2008, ApOpt, 47, 52
Willstrop, R. V. 1984, MNRAS, 210, 597
Woods, D. 2012, in Advanced Maui Optical and Space Surveillence Technologies Conference, The Space Surveillance Telescope: Focus and Alignment of a Three Mirror Telescope (Maui, HI: Maui Economic Development Board), 213